communications physics

Article

https://doi.org/10.1038/s42005-024-01585-x

Ultrafast quantum control of atomic excited states via interferometric two-photon Rabi oscillations

Yudong Chen[1,4], Sainan Peng[1,4], Zongyuan Fu[1], Liyang Qiu[1], Guangyu Fan[2], Yi Liu[2], Saijun Wu[1], Xinhua Xie[3] & Zhensheng Tao[1]

Quantum-state manipulation through coherent interaction with a radiation field is a fundamental process with broad implications in quantum optics and quantum information processing. However, current quantum control methods are limited by their operation at Rabi frequencies below the gigahertz range, which restricts their applicability to systems with long coherence times. To overcome this limitation, alternative approaches utilizing ultrafast driving lasers have garnered great interest. In this work, we demonstrate two-photon Rabi oscillations in the excited states of argon operating at terahertz frequencies driven by ultrafast laser pulses. Leveraging quantum-path interferometry, we are able to measure and manipulate both the amplitudes and phases of the transition dipoles by exploiting the intensity and polarization state of the driving laser. This precise control enables femtosecond population transfer and coherent accumulation of geometric phase. Our findings provide valuable insights into the all-optical manipulation of extreme-ultraviolet radiations and demonstrate the possibility of ultrafast quantum control through interferometric multiphoton transitions.

Coherent interaction with a radiation field drives population transfer between a two-level system, resulting in Rabi oscillations[1]. This fundamental process is critical for quantum-state manipulation and underpins a variety of implementations in quantum optics and quantum information processing[2–4]. To achieve coherent quantum control, it is imperative to ensure a light-matter interaction that occurs within sufficiently short timescales, before the decay of coherence[5,6]. Currently, coherent quantum control predominantly relies on continuous waves in the microwave, infrared, and visible regions, typically operating with Rabi frequencies below the gigahertz range[6,7]. This limitation considerably restricts the applicability of quantum control to systems with long coherence times, such as meta-stable atomic spins[8–10] and superconducting qubits[11,12]. To overcome this limitation, it is preferable to employ intense ultrafast lasers to drive Rabi oscillations on picosecond or even femtosecond timescales[13], manipulating the population and phase of quantum states in rapidly decohering systems. It is expected that increasing the Rabi frequency by using high-intensity ultrafast lasers would accelerate quantum operations. However, it is essential to consider nontrivial processes induced by high laser intensities and the broad bandwidth of ultrafast laser pulses, such as AC Stark shifts[14,15], multiphoton transitions[16] and complex multi-level coupling, for effective quantum control.

Extending Rabi oscillations to the multiphoton regime presents new possibilities for accessing quantum control of highly excited and dipole-forbidden dark states. Previous investigations on multiphoton quantum control using ultrashort laser pulses have attracted great attention. For instance, femtosecond vacuum ultraviolet laser pulses have been used to induce two-photon Rabi oscillations in krypton atoms[17], and step-ladder Rabi oscillations in H_2[18], resulting in population transfer. Suppression of ionization probability due to Rabi oscillations has been observed in the resonant two-photon ionization of He driven by extreme-ultraviolet (XUV) free-electron lasers[19,20]. By using advanced pulse shaping techniques, the switching between photon absorption and no absorption by Cs atoms was demonstrated through non-resonant two-photon excitation[16,21]. Moreover, intense ultrafast lasers have been employed to manipulate specific chemical dissociation processes and control the branch ratios between different reaction channels of polyatomic molecules, through both multiphoton excitation and Stark shifting effects induced by intense femtosecond laser pulses[22]. The interference between a one-photon transition induced by second-harmonic light and a two-photon transition induced by

[1]State Key Laboratory of Surface Physics, Key Laboratory of Micro and Nano Photonic Structures (MOE), and Department of Physics, Fudan University, Shanghai 200433, China. [2]Shanghai Key Lab of Modern Optical System, University of Shanghai for Science and Technology, Shanghai 200093, China. [3]SwissFEL, Paul Scherrer Institute, Villigen PSI 5232, Switzerland. [4]These authors contributed equally: Yudong Chen, Sainan Peng. e-mail: zhenshengtao@fudan.edu.cn

fundamental light was utilized to coherently control dissociative ionization of molecules[23–25]. More recently, Freeman resonance[26] induced by a strong laser field was utilized to support two-photon Rabi oscillations with terahertz (THz) frequencies[27]. Previous studies have dominantly focused on coherent optical control of level populations, but limited emphasis has been placed on phase control. The precise control of quantum phases under strong-field driving can enable electron localization via quantum mechanical interference during molecular photoionization[28–30], as well as reconstruction of laser-driven quantum states through photoelectron holographic imaging[31–33].

In this work, we employ quantum-path interferometry (QPI) to achieve phase measurements and demonstrate control of two-photon Rabi oscillations between excited states of argon driven by femtosecond laser pulses. The QPI technique involves the manipulation of two-photon pathways connecting a coherently prepared initial-state pair and a final state, resulting in delay-dependent oscillations of the final-state population, characterized by the emission of free-induction decay (FID) in the XUV wavelengths. The phase information of the Rabi pathways is encoded in the FID oscillations, enabling us to quantitatively monitor the coherent control of the dipole phases. Our results demonstrate THz-frequency Rabi oscillations driven by near-resonant femtosecond laser pulses, leading to both femtosecond population transfer and coherent accumulation of geometric phase. Furthermore, we demonstrate optical control of the amplitudes and phases of different transition dipoles using the intensity and polarization of the control pulses, as verified by a multi-level theoretical model. Our findings provide insights into the all-optical manipulation of XUV radiations and demonstrate the possibility for ultrafast quantum control of both amplitudes and phases through interferometric multiphoton transitions.

Results and discussion

Experimental results

The schematic of the experimental setup is illustrated in Fig. 1a. In our experiment, we first prepare the $3p^5 4s$ state in argon, located about 11.63 eV above the ground state ($|g\rangle$, $3p^6$), through a five-photon transition using a linearly polarized strong preparation pulse with a central wavelength of 520 nm ($\hbar\omega_{prep} = 2.38$ eV). The argon gas is in a gas cell with an inner diameter of 1.5 mm and a pressure of 26 kPa. Subsequently, a linearly polarized weak control pulse with a central wavelength of 1040 nm ($\hbar\omega_c = 1.19$ eV) is used to manipulate the excited states of argon. The control pulse is delivered at a time delay of τ relative to the preparation pulse, with its polarization at an angle of θ relative to that of the preparation pulse (Fig. 1a). The full-width-at-half-maximum (FWHM) duration of the control pulse is approximately 25 fs, which is determined by second-harmonic-generation (SHG) frequency-resolved optical gating (FROG)[34]. The duration of the preparation pulse is about 50 fs, on the other hand, estimated with the bandwidth of its spectrum and the dispersion induced by the vacuum

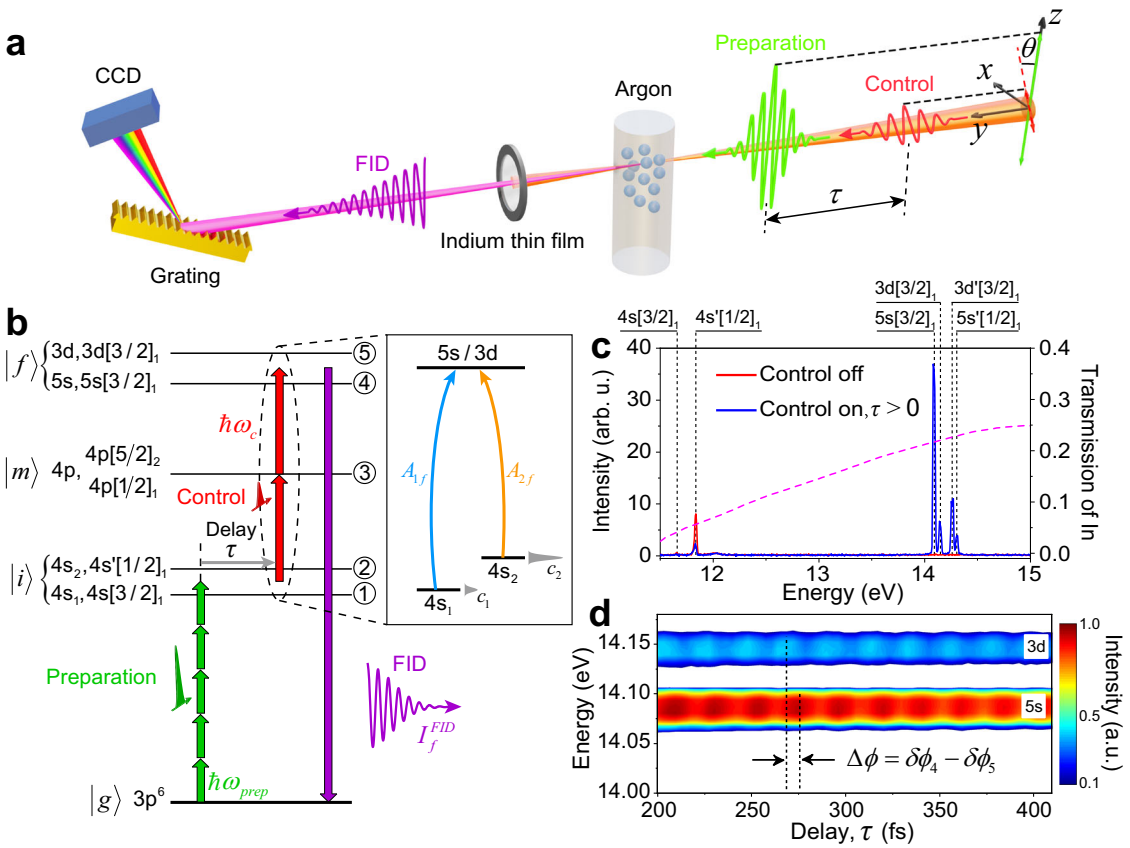

Fig. 1 | Experimental setup and concept illustration. a Schematic of the experimental setup. Argon gas in a gas cell is excited by a sequential preparation and control pulse pair with a time delay of τ. The free induction decay (FID) emission from the excited argon atoms is recorded by an XUV spectrometer composed of a grating and an XUV charge-coupled device (CCD) camera. The preparation and control pulses are blocked by an indium thin film. **b** Schematic of the energy level diagram of argon. The initial states ($|i\rangle$, $4s_1$ and $4s_2$) of the five-level system is first prepared by a strong laser pulse (green) with a five-photon process. The two-photon transitions from the initial states to the final states ($|f\rangle$, 5s and 3d) are then driven by a weak control pulse (red) under the near-resonant condition, facilitated by the intermediate states ($|m\rangle$, 4p). The relaxation from $|f\rangle$ to the ground state ($|g\rangle$, 3p) leads to the emission of FID (purple) with intensity of I_f^{FID}. Inset: Simplified illustration of the two-photon transitions from $4s_1$ and $4s_2$ to the 5s and 3d final states, leading to quantum-path interferometry (QPI) on the final states. **c** The XUV spectra of the FID emission with (blue line) and without (red line) control-pulse excitation. The peaks of different initial and final states are labeled. The transmission spectrum of the indium thin film is also plotted[62]. **d** The FID intensity of the 5s and 3d states as a function of the relative time delay between the prepare and control pulses τ. The relative phase between the two oscillation traces is labeled as $\Delta\phi$. The low-intensity regions are labeled by the white color for illustration purpose.

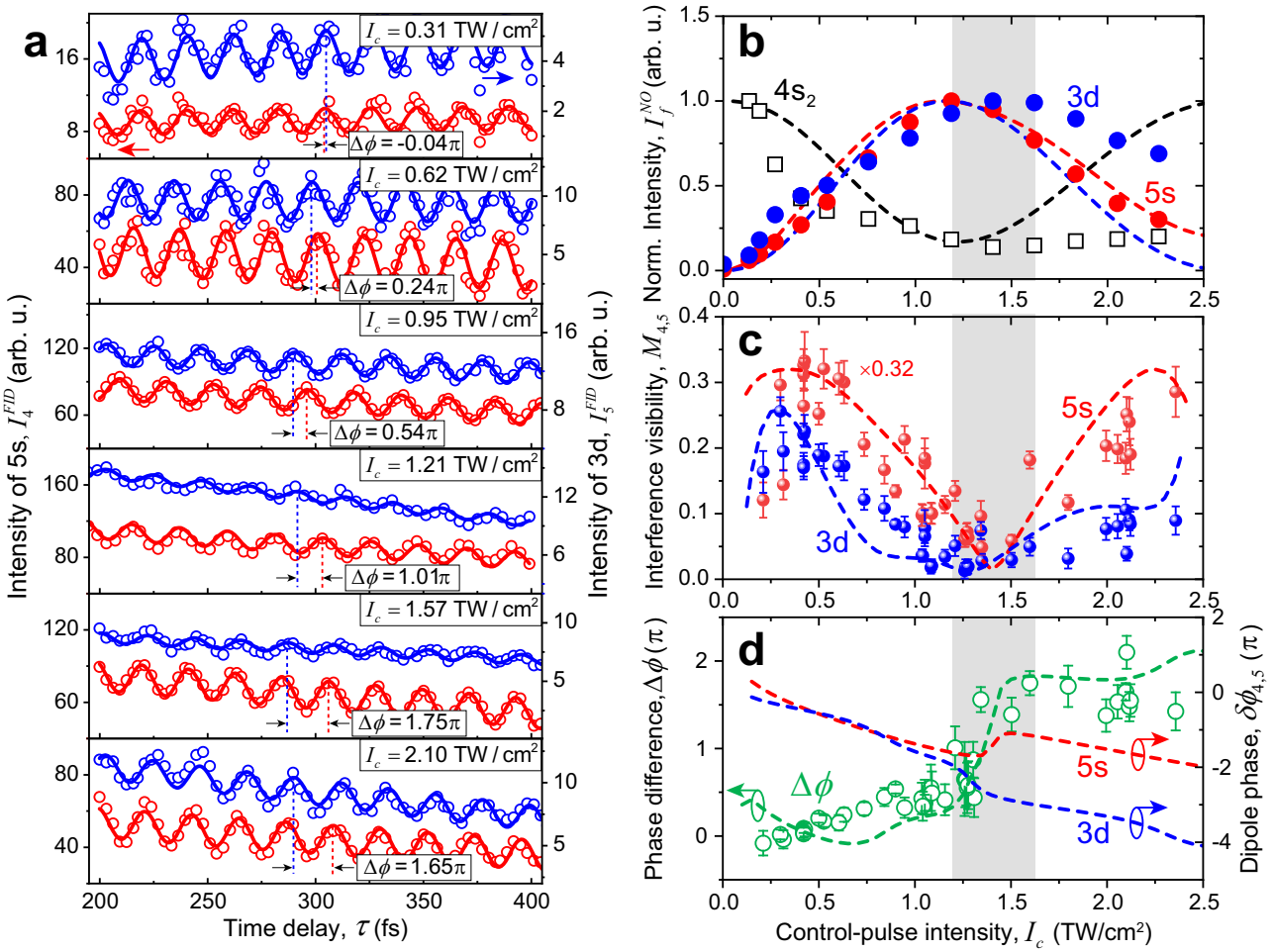

Fig. 2 | Control of quantum-path interferometry on different final states. a The experimental results of the FID-intensity oscillation of the 5s (blue) and 3d (red) states under different control-pulse intensities, I_c, with the relative phases between the two states $\Delta\phi$ are labeled. **b** The non-oscillating intensities I_f^{NO} of the FID from $4s_2$, 5s and 3d states as a function of I_c. The symbols represent the experimental results, while the dashed lines show the simulation results of the five-level model. **c** The interference visibility of the 5s and 3d states (M_4 and M_5, respectively) as a function of I_c. The dashed lines show the simulation results of the five-level model. The model results for the 5s state is scaled by 0.32 for comparison. **d** The relative difference of the oscillation phases of the 5s and 3d states, $\Delta\phi$, as a function of I_c. The dashed lines are the results of the five-level model simulations. The model results of the individual oscillation phases of the 5s and 3d states ($\delta\phi_4$ and $\delta\phi_5$, respectively) are also shown. The error bars in **c** and **d** are determined by considering both the fitting errors and the standard deviations of experimental results, extracted from 5 individual scans.

window. The preparation pulse is focused to a $1/e^2$ beam radius of about 20 μm, whereas the beam radius of the control pulse is about 70 μm. Both of them are measured by precisely imaging the focal point outside the vacuum chamber with a CCD camera. The distinct beam radii allow us to prepare the $3p^5 4$ s argon atoms in a small volume at the center of the control pulse, ensuring a uniform control-field intensity distribution within the interaction volume. The intensity of the preparation laser pulse is estimated to be 200 TW cm^{-2}, whereas the intensity of the control field (I_c) is much weak, varying below 3 TW cm^{-2}. The coherent excitation of the prepare-control pulses eventually leads to XUV FID that is recorded by an XUV spectrometer. More details about the experimental setup can be found in Methods and Supplementary Note 1.

In Fig. 1b, we present the energy-level diagram of the prepare-control scheme in our experiment. Due to *LS* coupling, there is a strong mixing of the transitory 4s states, $4s[3/2]_1$ and $4s'[1/2]_1$, which we label as $4s_1$ and $4s_2$ respectively, for convenience. In this context, we adopt the Racah notation[35,36] for a singly excited atom: $nl[K]_J$ and $nl'[K]_J$. Here, nl represents the principal and orbital quantum numbers of the excited electron, with nl and nl' respectively denoting the electronic core states of $^2P_{3/2}$ and $^2P_{1/2}$, K is the quantum number for an intermediate angular momentum, and the subscript J represents the quantum number for the total angular momentum. More details about the Racah notation can be found in Supplementary Note 11.

The weak control pulse drives two-photon transitions between the initial states 4s ($|i\rangle$) and the final states 5s ($5s[3/2]_1$) and 3d ($3d[3/2]_1$) ($|f\rangle$), facilitated by the intermediate state 4p ($|m\rangle$). The final states 5s and 3d are located at 2.26 and 2.32 eV above the $4s_2$ state, respectively, thus close to the two-photon resonance of the control pulse. In addition, the intermediate state involves $4p[1/2]_1$ and $4p[5/2]_2$ with energy levels positioned 1.08 and 1.27 eV above the $4s_2$ state, respectively[37,38]. In Fig. 1c, we plot the XUV spectrum of argon excited only by the preparation pulse (red line), which contains the FID signals solely from the $4s_1$ and $4s_2$ states. The FID intensity from the $4s_1$ state is more than one order of magnitude weaker than that from the $4s_2$ state, indicating a low population on $4s_1$ following the preparation-pulse excitation. This is mainly because the five-photon transition of the 520-nm preparation pulse better covers the $4s_2$ state compared to the $4s_1$ state (see Supplementary Note 2). The background-free FID signals from the 5s and 3d states only appear when the control pulse comes at a time delay of τ after the preparation pulse, accompanied by a decrease of the $4s_2$ intensity (blue line in Fig. 1c).

Furthermore, as illustrated in the inset of Fig. 1b, the control pulse interacts with the coherently prepared superposition of the $4s_1$ and $4s_2$

states. The interference between the two quantum paths connecting the two initial states ($4s_1$ and $4s_2$) and the same final state (5s or 3d) leads to oscillation in the population, and hence the FID intensities, of the 5s and 3d states as a function of the time delay τ, as shown in Fig. 1d. The phase information of the involved 4 s states and the two-photon dipole transitions is encoded in these oscillations. Similar intensity oscillations have been observed in previous studies[39].

The minimum requirement to depict the QPI is a two-channel interference theory (see Fig. 1b). The complex amplitude of the final state $|f\rangle$ populated through two-photon transition from the initial state $|i\rangle$ (see Fig. 1b), driven by the control pulse at a time delay of τ, is given by

$$A_{if}(\tau) = e^{-i\frac{E_i}{\hbar}\tau} a_{if} e^{-i\varphi_{if}} \tag{1}$$

Here, we use $i = 1, 2$ to denote the initial states $4s_1$ and $4s_2$, $f = 4, 5$ to denote the two final states 5s and 3d, and $m = 3$ to denote the intermediate state 4p. The corresponding field-free energies are E_i, E_m and E_f, respectively. a_{if} and φ_{if} represent the amplitude and the phase of the two-photon transition. The first term on the right-hand side of Eq. (1) represents the free-evolution phase of the $4s_1$ and $4s_2$ states before the arrival of the control pulse. The complex amplitude $a_{if}e^{-i\varphi_{if}}$ induced by the control pulse can be calculated by[40]

$$a_{if}e^{-i\varphi_{if}} = c_i(0)\left\langle f\left|\hat{T}e^{-i\int_0^\infty H(t_d)dt_d}\right|i\right\rangle \tag{2}$$

where $t_d = t - \tau$ and t represents time, the coefficient $c_i(0)$ is the initial amplitude of the $4s_i$ state, $\hat{T}$ is time-ordering operator. The interaction Hamiltonian $H(t_d)$ is given by $H(t_d) = H_0 + V(t_d)$, where H_0 is the field-free Hamiltonian and $V(t_d)$ represents the interaction of the control pulse with the five-level quantum system [$i = 1, 2$; $m = 3$; $f = 4, 5$]. More detailed derivation can be found in Supplementary Note 3.

The intensity of the FID emission from $|f\rangle$ is proportional to $|A_{1f}(\tau) + A_{2f}(\tau)|^2$:

$$\begin{aligned} I_f^{\mathrm{FID}}(\tau) \propto \left|A_{1f}(\tau) + A_{2f}(\tau)\right|^2 &= \left|a_{1f}\right|^2 + \left|a_{2f}\right|^2 \\ &+ 2|a_{1f}||a_{2f}|\cos(\omega\tau + \delta\phi_f) \end{aligned} \tag{3}$$

The first two terms on the right-hand side represent the non-oscillating part of the FID intensity $I_f^{\mathrm{NO}} = |a_{1f}|^2 + |a_{2f}|^2$, and the third term leads to intensity oscillations at a frequency of ω, where the value of ω is determined by the energy separation between the $4s_1$ and $4s_2$ states: $\omega = (E_2 - E_1)/\hbar$. The difference of the dipole-transition phases between the two quantum paths is imprinted in the oscillation phase by $\delta\phi_f = \varphi_{2f} - \varphi_{1f}$. As shown in Fig. 1d, the period of oscillation is approximately 21.8 fs, which is consistent with $E_2 - E_1 \approx 0.20$ eV. A phase difference between the 5s and 3d signals ($\Delta\phi = \delta\phi_4 - \delta\phi_5$) can be clearly resolved.

The QPI method allows to retrieve the amplitude and phase information of the two quantum paths and therefore enables us to investigate the influence of the control pulse on the two-photon transition dipoles in the five-level system (Fig. 1b). In Fig. 2a, we show the FID intensities from the 5s and 3d states as a function of τ for different control-pulse intensities (I_c) in the time delay window between 200 and 400 fs. The polarization angle θ is fixed at 90° in these measurements. Under this condition, we expect the intermediate state $4p[1/2]_1$ is more likely to participate in the two-photon transition, given its proximity to the single-photon resonance from the 4 s states. Furthermore, our experiment reveals that the interference visibility (see below) remains a constant for time delays up to 2 ps, indicating a long coherence time of the prepared initial-state pair, while the non-oscillation intensities (I_f^{NO}) decays following the population decay on the 4 s states (see Supplementary Note 4). Thus, we believe that the conclusion obtained within different time delay windows remains consistent.

By fitting the oscillating signals with sinusoidal functions, we obtain the non-oscillating intensity (I_f^{NO}), the interference visibility ($M_f = \frac{2|a_{1f}||a_{2f}|}{|a_{1f}|^2+|a_{2f}|^2}$) and the phase difference ($\Delta\phi$) as a function of I_c, which are shown in Fig. 2b–d. Our results reveal that $I_{4,5}^{\mathrm{NO}}$ of the 5s and 3d states, as well as I_2^{NO} of the $4s_2$ state, exhibit a non-monotonic dependence on the control-laser intensity. Specifically, both I_4^{NO} and I_5^{NO} reach their maximum values at $I_c \approx 1.4$ TW cm^{-2}, while I_2^{NO} reaches its minimum. This indicates a controlled population transfer from the $4s_2$ states to the 5s and 3d excited states driven by the control pulse. It is important to note that the population prepared by I_{prep} on the $4s_1$ state is relatively low. Therefore, the transitions originating from the $4s_1$ state only contribute a small portion to the populations of the intermediate and final states (see Supplementary Note 2).

On the other hand, we observe that the interference visibility, M_4 and M_5, reach their minima at $I_c \approx 1.4$ TW/cm^2 (Fig. 2c), and, correspondingly, the phase difference $\Delta\phi$ exhibits a strong shift at the same intensity (Fig. 2d). These observations indicate that the control pulse not only influences the population transfer but also modulates the interference between the two quantum paths, consequently leading to a change in the relative phase of the oscillations.

Theoretical model

To gain further insight on the experimental observations, we employ a numerical approach to solve Eqs. (1)–(3). The time evolution of the system can be obtained by solving the Schrödinger equation

$$i\hbar\frac{\partial}{\partial t}\left|\psi(t)\right\rangle = H(t,\tau)\left|\psi(t)\right\rangle \tag{4}$$

Here, $|\psi(t)\rangle$ is the wavefunction of the five-level quantum system given by $|\psi(t)\rangle = \sum_{n=i,m,f} c_n(t)|n\rangle$, where c_n is the complex amplitude of state $|n\rangle$. The Hamiltonian $H(t,\tau)$ can be described by a 5×5 matrix:

$$H(t,\tau) = \begin{pmatrix} E_1 & 0 & \Omega_{13} & 0 & 0 \\ 0 & E_2 & \Omega_{23} & 0 & 0 \\ (\Omega_{13})^* & (\Omega_{23})^* & E_3 & \Omega_{34} & \Omega_{35} \\ 0 & 0 & (\Omega_{34})^* & E_4 & 0 \\ 0 & 0 & (\Omega_{35})^* & 0 & E_5 \end{pmatrix} \tag{5}$$

which characterizes the interaction between the control-laser field and the five-level system. The Rabi frequencies $\Omega_{13/23/34/35}$ are given by $\Omega_{13/23/34/35} = -E_c(t,\tau)d_{13/23/34/35}/\hbar$, where d_{13}, d_{23}, d_{34} and d_{35} are the transition dipoles between different states, and E_c represents the control-laser field. To account for the difference in the initial-state population on $4s_1$ and $4s_2$, we set the wavefunction of the five-level system at $t = 0$ to be $|\psi(0)\rangle = c_1(0)|4s_1\rangle + c_2(0)|4s_2\rangle$ with $c_1(0) \approx 0.37$ and $c_2(0) \approx 0.93$ (see Supplementary Note 2).

The complex amplitude $c_f(\tau)$ of the final states can be calculated by

$$\begin{aligned} c_f(\tau) &= \left\langle f\left|\hat{T}e^{-i\int_0^\infty H(t,\tau)dt}\right|\psi(0)\right\rangle \\ &= \sum_{i=1,2} c_i(0)e^{-i\frac{E_i}{\hbar}\tau}\left\langle f\left|\hat{T}e^{-i\int_0^\infty H(t_d)dt_d}\right|i\right\rangle, \end{aligned} \tag{6}$$

where $\hat{T}$ is the time-ordering operator. Consequently, the control-pulse-induced transition amplitudes from $|i\rangle$ to $|f\rangle$ in Eqs. (1) and (2) can be obtained.

We employ the Runge–Kutta method to numerically solve Eq. (6) and obtain the complex amplitude $c_f(\tau)$. The oscillations of the FID intensity (I_f^{FID}) as a function of time delay τ are obtained in the delay time window between 200 and 400 fs, during which the electrical field of the preparation pulse ceases to interact with the atoms. Then, the quantities I_f^{NO}, M_f and $\Delta\phi$

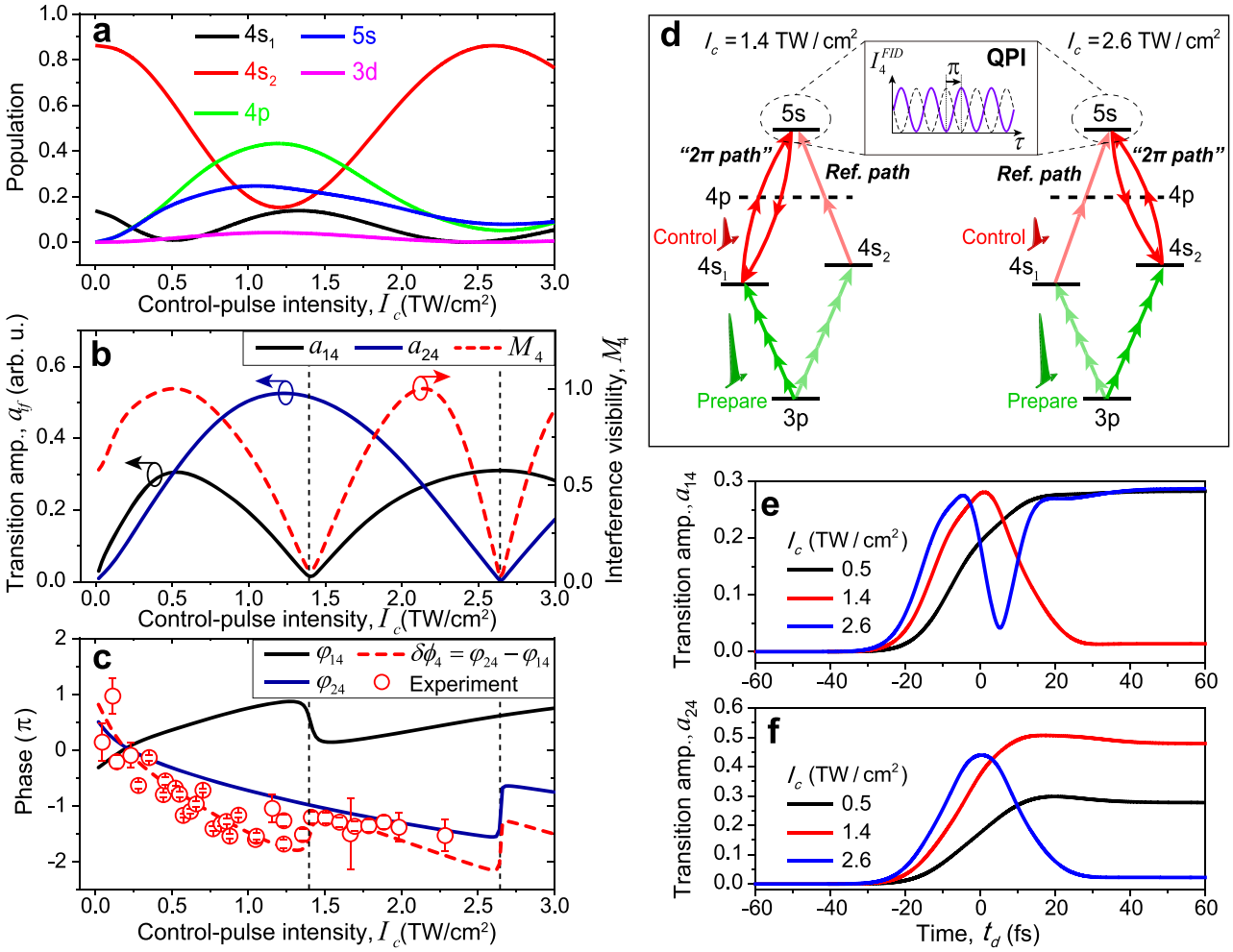

Fig. 3 | Transition amplitudes and phases involved in quantum-path interferometry of 5s. a Model results of the populations on different states under varying control-pulse intensity, I_c. **b** The model results of the transition amplitudes between the initial states and the 5s final state (a_{i4}), and the interference visibility M_4 as a function of the control pulse intensity, I_c. **c** The symbols represent the experimental results of the oscillating phase of the 5s state, $\delta\phi_4$. The error bars are determined by considering both the fitting errors and the standard deviations of experimental results, extracted from 5 individual scans. The solid lines show the model results of the phases of two-photon channels to the 5s state, φ_{i4}, and the dashed line represents the model results of the corresponding oscillating phase. **d** Illustration of the QPI on the 5s state under different control-laser intensity, I_c, showing the jump of the oscillating phase when the paths reach the "2π condition". **e** The time evolution of the transition amplitude a_{14} under different control-laser intensity, I_c. **f** Same as **e** for the transition amplitude a_{24}.

are extracted using the same data-analysis procedure applied to the experimental results. In order to achieve agreement between the model and our experimental results shown in Fig. 2b–d, we use the four dipole moments as fitting parameters. The comparison between the fitting results and the literature values[38,41] is summarized in Supplementary Table S2. The simulation results are presented as dashed lines in Fig. 2b–d, showing qualitative agreement with the experimental observations.

Here, we acknowledge that the values of I_f^{NO} cannot directly measure the populations on different final states because of the undetermined transition dipoles for the FID recombination, as well as the macroscopic phase-matching effect[42]. To facilitate the comparison in Fig. 2b, we normalize both the experimental and theoretical results to their respective maximum values. The overall agreement observed in the evolution of the experimental and theoretical results as a function of I_c corroborates our model. The detailed evolution of state populations is illustrated in Fig. 3a. More details about the numerical simulations can be found in the Supplementary Note 3.

In the simulation, by setting initial conditions $c_2(0) = 0$ or $c_1(0) = 0$, we can obtain the two-photon complex amplitudes $a_{1f}e^{-i\varphi_{1f}}$ and $a_{2f}e^{-i\varphi_{2f}}$, respectively, thus allowing to disentangle the contributions from individual transition channels. In Fig. 3b, we illustrate the results of our model for the transitions to the 5s final state. We observe that the diminish of the interference visibility M_4 at $I_c \approx 1.4$ TW cm^{-2} (Fig. 2c) is caused by the minimum value of the transition amplitude from $4s_1$ to 5s (a_{14}). This indicates that the control pulse with $I_c \approx 1.4$ TW cm^{-2} can drive ultrafast population transfer in this particular channel, completing one Rabi flop within approximately 60 fs (approximately the $1/e^2$ duration of the control pulse). The two-photon Rabi oscillation hence occurs with an effective frequency of $\Omega_{14}^{[2]}/2\pi \approx 1/(60\text{fs}) \approx 16.7$ THz. In contrast, the second channel ($4s_2 \rightarrow 4p \rightarrow 5s$), which dominates the population transfer, possesses only half of the same Rabi frequency reaching the "π-pulse condition" with the maximum of the transition amplitude at $I_c \approx 1.4$ TW cm^{-2}. The two-photon Rabi frequency of $\Omega_{24}^{[2]}/2\pi = 16.7$ THz is, on the other hand, reached when $I_c \approx 2.6$ TW cm^{-2} for this channel (Fig. 3b). This difference between the two channels is mainly caused by the smaller transition dipole between $4s_2$ and 4p when compared to that between $4s_1$ and 4p ($d_{23} < d_{13}$, see Supplementary Table S2 and Note 9).

Furthermore, as shown in Fig. 3c, we observe that the oscillation phase $\delta\phi_4$ of 5s gradually drifts as a function of I_c, and there exists a phase jump of ~π accompanied by the minimum of the transition dipole amplitude. These results are consistent with our experimental measurement of $\delta\phi_4$, for which a time-delay stabilization scheme was implemented (see Supplementary

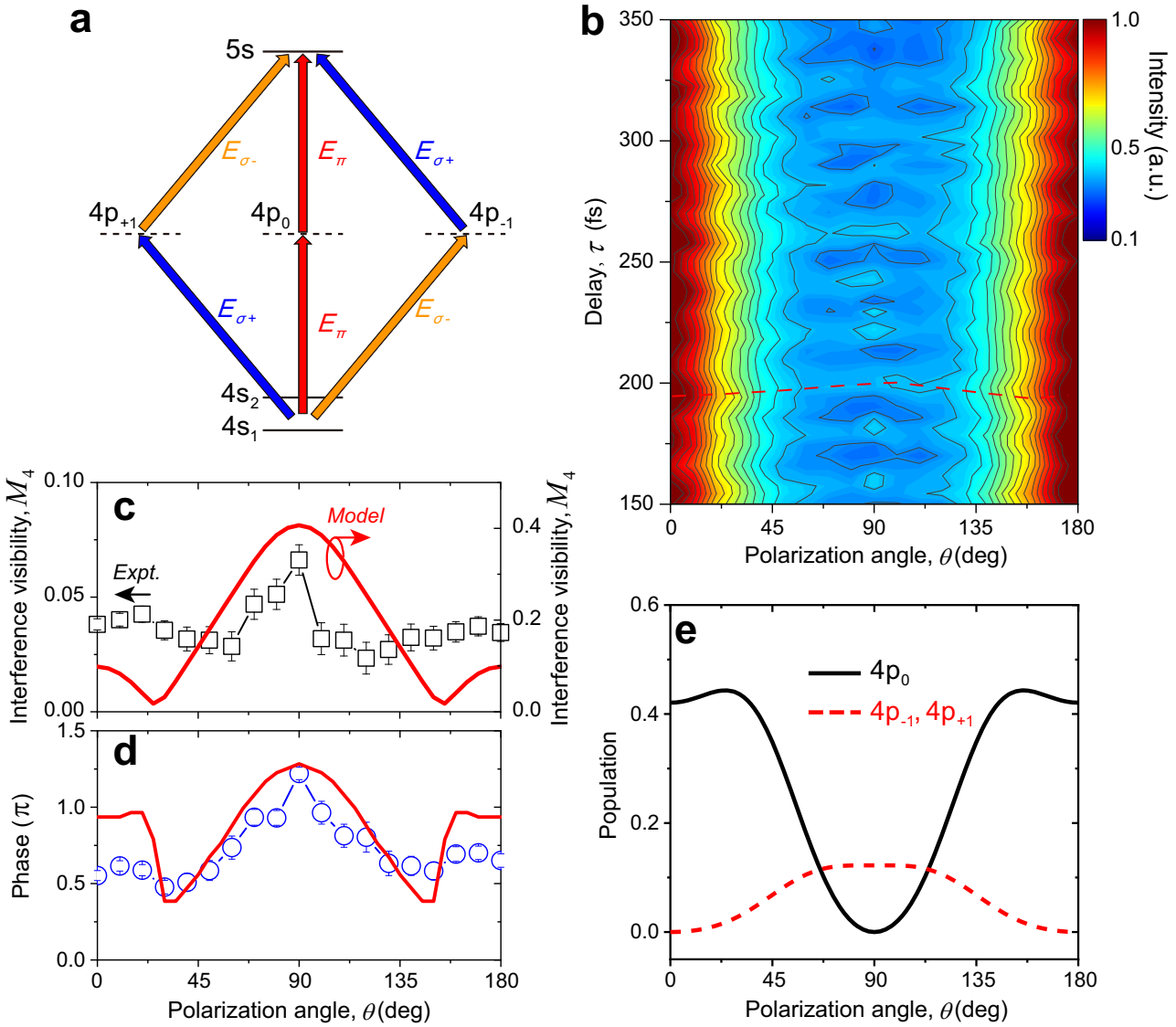

Fig. 4 | Polarization-dependent quantum manipulation of 5s. a Illustration of the polarization-dependent transitions in the multi-level quantum system. **b** The oscillation of I_4^{FID} as a function of delay τ under different polarization angle θ. The dashed red line illustrates the phase shift of the intensity oscillation. **c** The interference visibility M_4 as a function of θ. The red solid line represents the model results. **d** The oscillating phase of the 5s state $\delta\phi_4$ as a function of θ. The red solid line represents the model results. The error bars in **c** and **d** are determined by the fitting errors. **e** The model results of the population on the intermediate states of different magnetic sublevels M = 0, ±1.

Note 8). The observed phase shift of π at $I_c \approx 1.4$ TW cm^{-2} arises from the geometric phase accumulated during the cyclic $4s_1$-5s two-photon transition. In this cyclic transition, the $4s_1$ amplitude returns to the same state, acquiring a π geometric phase before additional 5s coupling during the Rabi oscillation[43,44]. This π-phase shift is subsequently detected through interference with the reference path 3p-$4s_2$-5s (see Fig. 3d), manifesting in the XUV FID emission signals. A second π-phase jump is expected at $I_c \approx 2.6$ TW cm^{-2}, corresponding to the "2π-pulse condition" for the two-photon transition between $4s_2$ and 5s, while the quantum path of 3p-$4s_1$-5s serves as the "reference path" in this case. Here, by utilizing the QPI between the "2π path" and the reference path that possesses a smooth phase variation (Fig. 3d), we are able to resolve the geometric phase in the measurements. Similar analysis can be applied to the 3d final state (see Supplementary Note 6). The abrupt phase shift of Δϕ in Fig. 2d is induced by the appearance of the consecutive "2π-pulse conditions" on the 5s and 3d states.

The time-evolution of transition amplitudes provides a clear evidence of Rabi oscillations in different transition channels. As depicted in Fig. 3e, f, we present the simulation results for a_{14} and a_{24}, respectively. The transition amplitude a_{14} exhibits oscillations as a function of time (t_d) with distinct Rabi frequencies, which vary with the control pulse intensity I_c. Under $I_c = 0.5$ TW cm^{-2}, the control pulse efficiently drives the transition from the $4s_1$ state to the 5s excited state, while the transition probability is minimized under the "2π-pulse condition" with $I_c = 1.4$ TW cm^{-2}, completing one Rabi flop within approximately 60 fs. By further increasing I_c to 2.6 TW cm^{-2}, the maximum transfer probability is achieved again under the "3π-pulse condition." In comparison, the channel of a_{24} possesses approximately half the Rabi frequency compared to a_{14}, owing to its smaller transition dipole values. More details about the Rabi oscillations in different transition channels can be found in Supplementary Note 5.

The overall population transfer to the excited states (5s and 3d) is determined by the coherent sum of the complex amplitudes from the $4s_1$ and $4s_2$ states driven by the control pulse, i.e. $|A_{1f}(\tau) + A_{2f}(\tau)|^2$. QPI leads to oscillations in the populations of different states as a function of the time delay τ. For clarity, we present the delay-averaged population, represented by the non-oscillating intensity (I_f^{NO}), and the corresponding results for different states are plotted in Fig. 3a. Our results highlight the importance of

multi-level coupling in the population dynamics. At an intensity of $I_c \approx 1.4$ TW cm^{-2}, approximately 70% of the total population is transferred away from the $4s_2$ state, while only approximately 25% is transferred to the 5s state, and a mere 4% to the 3d state, with approximately 40% of the total population remaining on the 4p intermediate state. More details about the population transfer can be found in Supplementary Note 7.

The population transfer through Rabi oscillation is strongly influenced by the intermediate state. To elucidate its effect, we conducted additional simulations by varying the energy of the 4p intermediate state (E_3), while keeping the values of transition dipoles fixed. The results are presented in Supplementary Fig. S10. We find that, when E_3 is below 12.80 eV, the population can be efficiently transferred from $4s_2$ to 5s with an overall efficiency approaching 70%, while the population remaining on the 4p intermediate state is minimal. On the other hand, when E_3 exceeds 13.10 eV, the population on 4p is also very low, but, in contrast, the efficiency of population transfers to 5s and 3d decreases, and more population stays on the $4s_2$ initial state. Only when the 4p intermediate state is close to the single-photon resonance from $4s_1$ and $4s_2$ (from 12.80 to 13.05 eV), there is high efficiency of population transfer to the 4p state, and the situation in our work falls in this range ($E_3 = 12.91$ eV). This result is consistent with previous work[45]. In Supplementary Fig. S11, we summarize the population transfer to different states at the control-pulse intensity when the $4s_2$ population reaches its minimum, which clearly shows this trend.

Under a strong field dressing, the AC Stark energy shifts of the excited states may introduce new resonant channels for above-threshold-ionization[15,46]. In our simulation, the AC Stark shifts induced by the control field are considered, resulting in energy shifts on the order of tens of meV (see Supplementary Fig. S13). Note that this energy shift is smaller than the bandwidth of the control pulses and also much smaller than the energy difference between the high-energy excited states (5s and 3d) and the ionization potential of argon. Consequently, we can conclude that ionization through new resonant channels, attributed to the ponderomotive shifting of excited states, is negligible in this study. Furthermore, given that FID emission typically occurs on a timescale of tens of ps[39], when the influence of the control-pulse field diminishes, the Autler-Townes splitting of the FID spectrum is absent. This stands in contrast to techniques such as attosecond transient absorption[47] or photoelectron spectroscopy[48], where atomic states under laser-field dressing are directly probed.

Coherent manipulation via laser polarization states

Except for the laser intensity, the two-photon Rabi oscillations can also be manipulated by the polarization state of the control pulse. Previously, coherent multi-photon control of atoms and molecules using the polarization states of driving lasers has been extensively studied[45,49,50]. With respect to the quantization axis ($\hat{z}$) along the polarization of the preparation laser field, the control-laser field can be decomposed as

$$\vec{E}_c = \vec{E}_\pi \cos\theta + \left(\vec{E}_{\sigma+} + \vec{E}_{\sigma-}\right)\frac{\sin\theta}{\sqrt{2}} \quad (7)$$

where $\vec{E}_\pi = E_c\hat{z}$, $\vec{E}_{\sigma+} = \frac{E_c}{\sqrt{2}}\left(\hat{x} + i\hat{y}\right)$ and $\vec{E}_{\sigma-} = \frac{E_c}{\sqrt{2}}\left(\hat{x} - i\hat{y}\right)$ represent the control-field components with different angular momentum. By varying θ, we selectively excite the two-photon transitions through different magnetic sublevels M = 0, ±1 of the 4p intermediate states (Fig. 4a), which leads to different dipole moments of the transition paths. In Fig. 4b, we plot the delay-dependent I_4^{FID} of the 5s state at different θ, with the control-laser intensity fixed at $I_c \approx 0.5$ TW cm^{-2}. In addition to the ω oscillation that results from QPI, we observe maximum FID intensity when the control-pulse polarization is aligned or anti-aligned with the preparation pulse ($\theta = 0$ or 180°), and minimum FID intensity when the polarizations are orthogonal ($\theta = 90°$). Furthermore, we can retrieve the interference visibility and phases as a function of the polarization angle from the measured data, which exhibit clear dependence on the polarization angle θ (Fig. 4c, d).

To explain these experimental observations, we extend the five-level model to a seven-level one by considering the magnetic sublevels of $4p_0$, $4p_{+1}$ and $4p_{-1}$, denoted as $m = 3$, 3' and 3", respectively. Taking into account the symmetry of the transition dipoles and the preparation-control laser fields, we anticipate that the transitions excited by the σ-components of the control field exhibit equal dipole moment strengths, specifically $d^{\sigma}_{i3'} = d^{\sigma}_{i3''}$ and $d^{\sigma}_{3'f} = d^{\sigma}_{3''f}$ (see Supplementary Note 10), and their values are provided d_{i3} and d_{3f}, respectively (see Supplementary Table S2). To achieve agreement with the experimental results, we assume that the strength of the dipole moments for the π-transitions are 1.6 times stronger than those for the σ-transitions, i.e., $d^{\pi}_{i3} = 1.6 \times d^{\sigma}_{i3'}$ and $d^{\pi}_{3f} = 1.6 \times d^{\sigma}_{3'f}$. This conclusion aligns with the experimentally observed stronger FID intensity at the π-transitions, and is also in accordance with previous work[27].

Here, we acknowledge that our model simplifies the consideration of the intermediate states and the 3d final state. Specifically, according to the selection rule, the transitions from the 4 s states to $4p[1/2]_1$ are forbidden when the control pulse contains only the π component ($\theta = 0$). Therefore, the intermediate state of $4p[5/2]_2$ is involved in the transition when $\theta = 0$, despite its larger single-photon detuning. By considering the involvement of the $4p[5/2]_2$ state, we estimate the ratio between the transition dipoles of the π transitions and the σ transitions to be approximately 1.98, providing qualitative support for our fitting result. Further details of the model can be found in Supplementary Note 10.

The simulation results qualitatively agree with the θ-dependent interference visibility (M_4) and phase ($\delta\phi_4$), as shown in Fig. 4b, c. The changes in M_4 and $\delta\phi_4$ under different θ angles can be attributed to the variation of the transition amplitudes of different channels with θ-dependent dipole strength and Rabi frequencies. The selective excitation of the $4p_0$ and $4p_{\pm1}$ channels by the $\vec{E}_\pi$ and $\vec{E}_{\sigma\pm}$ fields is also clearly shown by the model, as evidenced by the variation of the population transfer to the intermediate states, as shown in Fig. 4e.

Conclusions

In this work, we exploit multiphoton transitions induced by the preparation pulse to establish the populations on two initial states ($4s_1$ and $4s_2$). The coherent preparation of these two initial states offers a unique opportunity to observe quantum-path interference, a critical element for extracting the geometric phase in coherent light-matter interaction. However, we acknowledge that the multiphoton approach has inherent limitations in terms of the preparation efficiency of initial states. Furthermore, the requirement for an ultrashort, broadband laser pulse in the process poses challenges in achieving precise control over the initial quantum states. With the rapid development of bright XUV sources, such as high-harmonic generation[51,52] and free-electron lasers[53,54], there is now the potential to directly induce resonant transitions for the precise quantum-state preparation. Especially, coherent and ultrafast control of atoms and molecules using XUV lasers has become feasible in recent years[19,20,48,55–59].

In conclusion, our study demonstrates the successful application of ultrafast laser pulses to effectively control the amplitude and phase of two-photon Rabi oscillations in the excited states of argon. In particular, using the QPI method, we measure and further demonstrate the manipulation of both the amplitudes and phases of the dipoles associated with the two-photon transitions driven by femtosecond laser pulses. Our findings revealed THz Rabi oscillation frequencies under near-resonant excitation, facilitating femtosecond population transfer and the coherent accumulation of geometric phase. Furthermore, we establish that the control of the two-photon transition dipoles can be achieved through adjusting the intensity and polarization state of the control pulses, as validated by our multi-level theoretical model. Our study opens up new possibilities for exploring and manipulating the quantum dynamics of excited states in atoms and molecules. By using ultrafast laser pulses, we can achieve precise control of excited atoms using two-photon Rabi oscillations and the associated geometric phase. This could lead to novel applications in quantum information processing, spectroscopy, and metrology. Future work could extend our approach to other multiphoton transitions and more complex systems, such as molecules or solids.

Methods

Experimental setup

The experimental setup for the two-color prepare-control experiment is shown in Supplementary Fig. S1a. In the experiments, we employ a Yb:KGW laser amplifier, with a pulse duration of 170 fs with a central wavelength of 1030 nm. The output laser is sent into an all-solid-state free-space PLKM compressors, which compress the pulse to a FWHM pulse duration of 25 fs[60,61]. The pulse duration is determined by the SHG-FROG measurement, as shown in Supplementary Fig. S1d, e. Then, the compressed beam is split into two portions with a 90:10 near-IR beam splitter (BS). The high-energy arm (90%) is frequency doubled using a type-I barium borate (BBO) crystal. The fundamental laser beam is removed by a dichroic mirror (DM) and the second harmonic beam with a pulse duration of 50 fs is served as the preparation beam for the experiment. The laser beam from the low-energy arm (10%) serves as the control beam and the delay between the preparation and the control pulses is controlled using a delay line in the control branch. The laser power of the control beam is varied by rotating a half wave-plate before a linear polarizer, and the polarization state of the control beam is controlled by a second half wave-plate. The two arms are recombined using a dichroic mirror. The combined laser beam is then focused by a $f = 15$ cm lens into a gas cell with an inner diameter of 1.5 mm filled with argon gas. The backing pressure is set to be around 200 torr, which optimizes the brightness of the FID radiation. Within the interaction region, the intensity of the preparation laser pulse is estimated to be ~200 TW cm^{-2}, whereas the intensity of the control field (I_c) is much weak, varying below 3 TW cm^{-2}, which are determined by measuring the beam waist at the focus. The coherent excitation of the prepare-control pulses eventually leads to XUV FID that is recorded by an XUV spectrometer after blocking the driving laser beams using a 300 nm indium thin film. The transmission spectrum of the indium film is shown in Fig. 1c. In Supplementary Fig. S1b, c, we present the spectra of the control and preparation pulses, respectively.

Data availability

The authors confirm that the data supporting the findings of this study are available within the article and its supplementary materials. Additional data related to this paper may be requested from the authors.

Code availability

The authors confirm that the codes used in this study are available upon appropriate request.

Received: 12 September 2023; Accepted: 4 March 2024;
Published online: 16 March 2024

References

1. Rabi, I. I. Space quantization in a gyrating magnetic field. *Phys. Rev.* **51**, 652–654 (1937).
2. You, J. Q. & Nori, F. Superconducting circuits and quantum information. *Phys. Today* **58**, 42–47 (2005).
3. Nielsen, M. A. & Chuang, I. L. *Quantum Computation and Quantum Information* (Cambridge University Press, 2011).
4. Lukin, M. D. Colloquium: Trapping and manipulating photon states in atomic ensembles. *Rev. Mod. Phys.* **75**, 457–472 (2003).
5. He, Y. et al. Geometric Control of Collective Spontaneous Emission. *Phys. Rev. Lett.* **125**, 213602 (2020).
6. Huber, B. et al. GHz Rabi flopping to Rydberg states in hot atomic vapor cells. *Phys. Rev. Lett.* **107**, 243001 (2011).
7. Gentile, T. R., Hughey, B. J., Kleppner, D. & Ducas, T. W. Experimental study of one- and two-photon Rabi oscillations. *Phys. Rev. A* **40**, 5103–5115 (1989).
8. Saffman, M. Quantum computing with atomic qubits and Rydberg interactions: Progress and challenges. *J. Phys. B At. Mol. Opt. Phys.* **49**, 202001 (2016).
9. Barry, J. F. et al. Sensitivity optimization for NV-diamond magnetometry. *Rev. Mod. Phys.* **92**, 15004 (2020).
10. Wang, Y. et al. Single-qubit quantum memory exceeding ten-minute coherence time. *Nat. Photonics* **11**, 646–650 (2017).
11. Wu, Y. et al. Strong Quantum Computational Advantage Using a Superconducting Quantum Processor. *Phys. Rev. Lett.* **127**, 180501 (2021).
12. Devoret, M. H. & Schoelkopf, R. J. Superconducting Circuits for Quantum. *Science* **339**, 1169–1175 (2013).
13. Chew, Y. et al. Ultrafast energy exchange between two single Rydberg atoms on a nanosecond timescale. *Nat. Photonics* **16**, 724–729 (2022).
14. Rickes, T. et al. Efficient adiabatic population transfer by two-photon excitation assisted by a laser-induced Stark shift. *J. Chem. Phys.* **113**, 534–546 (2000).
15. Wiehle, R., Witzel, B., Helm, H. & Cormier, E. Dynamics of strong-field above-threshold ionization of argon: Comparison between experiment and theory. *Phys. Rev. A* **67**, 063405 (2003).
16. Meshulach, D. & Silberberg, Y. Coherent quantum control of multiphoton transitions by shaped ultrashort optical pulses. *Phys. Rev. A* **60**, 1287–1292 (1999).
17. Kittelmann, O., Ringling, J., Nazarkin, A., Korn, G. & Hertel, I. V. Direct observation of coherent medium response under the condition of two-photon excitation of krypton by femtosecond UV-Laser pulses. *Phys. Rev. Lett.* **76**, 2682–2685 (1996).
18. Palacios, A., Bachau, H. & Martín, F. Step-ladder Rabi oscillations in molecules exposed to intense ultrashort vuv pulses. *Phys. Rev. A* **74**, 031402(R) (2006).
19. Sato, T. et al. Determination of the absolute two-photon ionization cross section of He by an XUV free electron laser. *J. Phys. B At. Mol. Opt. Phys.* **44**, 161001 (2011).
20. Sako, T. et al. Suppression of ionization probability due to Rabi oscillations in the resonance two-photon ionization of He by EUV free-electron lasers. *Phys. Rev. A* **84**, 053419 (2011).
21. Meshulach, D. & Silberberg, Y. Coherent quantum control of two-photon transitions by a femtosecond laser pulse. *Nature* **396**, 239–242 (1998).
22. Levis, R. J., Menkir, G. M. & Rabitz, H. Selective bond dissociation and rearrangement with optimally tailored, strong-field laser pulses. *Science* **292**, 709–713 (2001).
23. Sheehy, B. & Walker, B. Phase control in the two-color photodissociation of HD. *Phys. Rev. Lett.* **74**, 4799–4802 (1995).
24. Ohmura, H., Nakanaga, T. & Tachiya, M. Coherent Control of Photofragment Separation in the Dissociative Ionization of IBr. *Phys. Rev. Lett.* **92**, 113002 (2004).
25. Thompson, M. R. et al. One and two-colour studies of the dissociative ionization and Coulomb explosion of H2 with intense Ti:sapphire laser pulses. *J. Phys. B At. Mol. Opt. Phys.* **30**, 5755–5772 (1997).
26. Freeman, R. R. et al. Above-threshold ionization with subpicosecond laser pulses. *Phys. Rev. Lett.* **59**, 1092–1095 (1987).
27. Fushitani, M. et al. Femtosecond two-photon Rabi oscillations in excited He driven by ultrashort intense laser fields. *Nat. Photonics* **10**, 102–105 (2016).
28. Gong, X. et al. Two-dimensional directional proton emission in dissociative ionization of H2. *Phys. Rev. Lett.* **113**, 203001 (2014).
29. Xie, X. et al. Zero-energy proton dissociation of H2+ through stimulated Raman scattering. *Phys. Rev. A* **99**, 043409 (2019).
30. Sansone, G. et al. Electron localization following attosecond molecular photoionization. *Nature* **465**, 763–766 (2010).
31. Blaga, C. I. et al. Imaging ultrafast molecular dynamics with laser-induced electron diffraction. *Nature* **483**, 194–197 (2012).
32. Smirnova, O. et al. High harmonic interferometry of multi-electron dynamics in molecules. *Nature* **460**, 972–977 (2009).
33. Gruson, V. et al. Attosecond dynamics through a Fano resonance: Monitoring the birth of a photoelectron. *Science* **354**, 734–738 (2016).
34. Trebino, R. et al. Measuring ultrashort laser pulses in the time-frequency domain using frequency-resolved optical gating. *Rev. Sci. Instrum.* **68**, 3277–3295 (1997).

35. Cowan, R. D. *The Theory of Atomic Structure and Spectra* (University of California Press, 1981).
36. Lengyel, B. A. *Lasers* (Wiley-Interscience, 1971).
37. Minnhagen, L. Spectrum and the energy levels of neutral argon, Ar I. *J. Opt. Soc. Am.* **63**, 1185–1198 (1973).
38. Zatsarinny, O. & Bartschat, K. B-spline calculations of oscillator strengths in neutral argon. *J. Phys. B At. Mol. Opt. Phys.* **39**, 2145–2158 (2006).
39. Beaulieu, S. et al. Phase-resolved two-dimensional spectroscopy of electronic wave packets by laser-induced XUV free induction decay. *Phys. Rev. A* **95**, 041401 (2017).
40. Cao, W., Warrick, E. R., Neumark, D. M. & Leone, S. R. Attosecond transient absorption of argon atoms in the vacuum ultraviolet region: Line energy shifts versus coherent population transfer. *New J. Phys.* **18**, 13041 (2016).
41. Wiese, W. I., Bridges, J. M., Kornblith, R. L. & Kelleher, D. E. Transition Probabilities for Prominent Ar I Lines in the Near Infrared. *J. Opt. Soc. Am.* **59**, 1206–1212 (1969).
42. Chini, M. et al. Coherent phase-matched VUV generation by field-controlled bound states. *Nat. Photonics* **8**, 437–441 (2014).
43. Berry, M. V. Quantal phase factors accompanying adiabatic changes. *Proc. R. Soc. Lond. A* **392**, 45–57 (2017).
44. Aharonov, Y. & Anandan, J. Phase change during a cyclic quantum evolution. *Phys. Rev. Lett.* **58**, 1593–1596 (1987).
45. Dudovich, N., Oron, D. & Silberberg, Y. Quantum Control of the Angular Momentum Distribution in Multiphoton Absorption Processes. *Phys. Rev. Lett.* **92**, 103003 (2004).
46. Schyja, V., Lang, T. & Helm, H. Channel switching in above-threshold ionization of xenon. *Phys. Rev. A* **57**, 3692–3697 (1998).
47. Wu, M., Chen, S., Gaarde, M. B. & Schafer, K. J. Time-domain perspective on Autler-Townes splitting in attosecond transient absorption of laser-dressed helium atoms. *Phys. Rev. A* **88**, 043416 (2013).
48. Nandi, S. et al. Observation of Rabi dynamics with a short-wavelength free-electron laser. *Nature* **608**, 488–493 (2022).
49. Brixner, T. et al. Quantum control by ultrafast polarization shaping. *Phys. Rev. Lett.* **92**, 208301 (2004).
50. Oron, D., Dudovich, N. & Silberberg, Y. Femtosecond Phase-and-Polarization Control for Background-Free Coherent Anti-Stokes Raman Spectroscopy. *Phys. Rev. Lett.* **90**, 213902 (2003).
51. Agostini, P. & DiMauro, L. F. The physics of attosecond light pulses. *Reports Prog. Phys.* **67**, 813–855 (2004).
52. Rundquist, A. et al. Phase-matched generation of coherent soft x-rays. *Science* **280**, 1412–1415 (1998).
53. Andruszkow, J. et al. First observation of self-amplified spontaneous emission in a free-electron laser at 109 nm wavelength. *Phys. Rev. Lett.* **85**, 3825–3829 (2000).
54. Wabnitz, H. et al. Multiple ionization of atom clusters by intense soft X-rays from a free-electron laser. *Nature* **420**, 482–485 (2002).
55. Cui, J. J. et al. Proposal for Observing XUV-Induced Rabi Oscillation Using Superfluorescent Emission. *Phys. Rev. Lett.* **131**, 43201 (2023).
56. Rohringer, N. & Santra, R. Resonant Auger effect at high x-ray intensity. *Phys. Rev. A* **77**, 053404 (2008).
57. Maroju, P. K. et al. Attosecond coherent control of electronic wave packets in two-colour photoionization using a novel timing tool for seeded free-electron laser. *Nat. Photonics* **17**, 200–207 (2023).
58. Prince, K. C. et al. Coherent control with a short-wavelength free-electron laser. *Nat. Photonics* **10**, 176–179 (2016).
59. Kanter, E. P. et al. Unveiling and driving hidden resonances with high-fluence, high-intensity X-ray pulses. *Phys. Rev. Lett.* **107**, 233001 (2011).
60. Zhu, B. et al. Spatially homogeneous few-cycle compression of Yb lasers via all-solid-state free-space soliton management. *Opt. Express* **30**, 2918–2932 (2022).
61. Zhang, S. et al. Solitary beam propagation in periodic layered Kerr media enables high-efficiency pulse compression and mode self-cleaning. *Light Sci. Appl.* **10**, 53 (2021).
62. Henke, B. L., Gullikson, E. M. & Davis, J. C. X-Ray interactions: photoabsorption, scattering, transmission, and reflection at E = 50-30,000 eV, Z = 1-92. *At. Data Nucl. Data Tables* **54**, 181–342 (1993).

Acknowledgements

This work was accomplished in Fudan University. We appreciate valuable discussions with Lei Geng, Zengxiu Zhao, Xiaowei Wang and Guangru Bai. Z.T. gratefully acknowledges support from the National Key Research and Development Program of China (Grant Nos. 2021YFA1400200 and 2022YFA1404700), the National Natural Science Foundation of China (Grant No. 12221004) and the Shanghai Municipal Science and Technology Basic Research Project (Grant No. 19JC1410900). S.W. acknowledges support from the National Natural Science Foundation of China (Grant No. 12074083) and the National Key Research and Development Program of China (Grant No. 2022YFA1404204). Y.L. acknowledges support from the National Natural Science Foundation of China (Grants No. 12034013). G.F. acknowledges support from the National Natural Science Foundation of China (Grants No. 12374318).

Author contributions

Z.T. and X.X. conceived the project. Y.C., S.P., Z.F. and L.Q. conducted the experiments, analyzed the data and performed the numerical simulations. G.F. and Y.L. provided technical support. L.Q., S.W. and X.X. provided theory support. Y.C., Z.T. and S.P. wrote the manuscript with the inputs from the other authors. All authors discussed the results and commented on the refined manuscript.

Competing interests

The authors declare no competing interests.

Additional information

Supplementary information The online version contains supplementary material available at https://doi.org/10.1038/s42005-024-01585-x.

Correspondence and requests for materials should be addressed to Zhensheng Tao.

Peer review information *Communications Physics* thanks the anonymous reviewers for their contribution to the peer review of this work. A peer review file is available.